Improved El Niño forecasting by cooperativity detection

Josef Ludescher[a], Avi Gozolchiani[b], Mikhail I. Bogachev[a,c], Armin Bunde[a], Shlomo Havlin[b], and Hans Joachim Schellnhuber[d,e,1]

[a]Institut für Theoretische Physik, Justus-Liebig-Universität Giessen, 35392 Giessen, Germany; [b]Department of Physics, Bar-Illan University, Ramat Gan 52900, Israel; [c]Radio Systems Department, St. Petersburg Electrotechnical University, St. Petersburg 197376, Russia; [d]Potsdam Institute for Climate Impact Research, 14412 Potsdam, Germany; and [e]Santa Fe Institute, Santa Fe, NM 87501

Contributed by Hans Joachim Schellnhuber, May 30, 2013 (sent for review March 12, 2013)

Although anomalous episodic warming of the eastern equatorial Pacific, dubbed El Niño by Peruvian fishermen, has major (and occasionally devastating) impacts around the globe, robust forecasting is still limited to about 6 mo ahead. A significant extension of the prewarning time would be instrumental for avoiding some of the worst damages such as harvest failures in developing countries. Here we introduce a unique avenue toward El Niño prediction based on network methods, inspecting emerging teleconnections. Our approach starts from the evidence that a large-scale cooperative mode—linking the El Niño basin (equatorial Pacific corridor) and the rest of the ocean—builds up in the calendar year before the warming event. On this basis, we can develop an efficient 12-mo forecasting scheme, i.e., achieve some doubling of the early-warning period. Our method is based on high-quality observational data available since 1950 and yields hit rates above 0.5, whereas false-alarm rates are below 0.1.

climate | cross-correlations | dynamic networks | ENSO | spring barrier

The so-called El Niño-Southern Oscillation (ENSO) is the most important phenomenon of contemporary natural climate variability (1–4). It can be perceived as a self-organized dynamical see-saw pattern in the Pacific ocean-atmosphere system, featured by rather irregular warm (El Niño) and cold (La Niña) excursions from the long-term mean state. ENSO has considerable influence on the climatic and environmental conditions in its core region, but affects also distant parts of the world. The pattern is causing disastrous flooding in countries like Peru and Ecuador as well as heavy droughts in large areas of South America, Indonesia, and Australia. It is arguably also associated with severe winters in Europe, anomalous monsoon dynamics in East Asia, intensity of tropical cyclones such as hurricanes in the Caribbean, and epidemic diseases occurring in a variety of places (5–9).

Strong El Niño events, in particular, have affected, time and again, the fate of entire societies. A popular, yet quite informative account of ENSO's destructive power is provided in ref. 10. This book investigates the pertinent droughts in India, China, and Brazil toward the end of the 19th century, which killed an estimated 30–50 million people.

What happened in premodern times is unlikely to be repeated in the future. However, anthropogenic global warming (11, 12) may have a significant effect on the character of ENSO and render this geophysical pattern even more challenging for certain societies. In fact, the phenomenon is listed among the so-called "tipping elements" in the Earth System (13, 14) that might be transformed—sooner or later—by the greenhouse-gas emissions from fossil-fuel burning and land-cover change. The scientific jury is still out, pondering the question of how El Niño events will behave in a world without aggressive climate-protection measures (15). Will the eastern tropical Pacific warm permanently, periodically, or as irregularly as nowadays? Will the oscillation go away completely (something that appears rather unlikely according to the recent assessment by Wang et al. in ref. 4) or gain in strength (as suggested by some paleo-climatic data)? In the latter case, anything that helps to improve the predictive power of the scientific ENSO analysis would be even more important than it is already today.

The ENSO phenomenon is currently tracked and quantified, for example, by the NINO3.4 index, which is defined as the average of the sea-surface temperature (SST) anomalies at certain grid points in the Pacific (Fig. 1). An El Niño episode is said to occur when the index is above 0.5 °C for a period of at least 5 mo. Sophisticated global climate models taking into account the atmosphere–ocean coupling as well as dynamical systems approaches, autoregressive models, and pattern-recognition techniques applied on observational and reconstructed records have been used to forecast the pertinent index with lead times between 1 and 24 mo. Up to 6 mo, the various forecasts perform reasonably well, whereas for longer lead times the performance becomes rather low (16–29). A particular difficulty for prediction of the NINO3.4 index is the "spring barrier" (see, e.g., ref. 30). During boreal springtime, anomalies that develop randomly in the western Pacific reduce the signal-to-noise ratio for the dynamics relevant to ENSO and make it harder to predict across the barrier.

In this study, we follow a different route. Instead of considering the time dependence of climate records at single grid points i, we study the time evolution of the interactions (teleconnections) between pairs of grid points i and j, which are represented by the strengths of the cross-correlations between the climate records at these sites. The interactions can be considered as links in a climate network where the nodes are the grid points (31–34). Recent empirical studies have shown that in the large-scale climate network the links tend to weaken significantly during El Niño episodes, and this phenomenon is most pronounced for those links that connect the "El Niño basin" (solid circles in Fig. 1) with the surrounding sites in the Pacific ocean (open symbols in Fig. 1) (the El Niño basin considered here consists of the NINO1, NINO2, NINO3, and NINO3.4 regions plus one grid point south of the NINO3.4 region) (32, 33).

Therefore, we concentrate on these links and show that well before an El Niño episode their mean strength tends to increase. We use this robust observation to forecast El Niño development more than 1 y in advance. We use the time span between 1950 and 2011, where the information on ENSO dynamics is reliable and the observational data necessary for constructing the climate network are complete (35).

We use the network shown in Fig. 1, which consists of 14 grid points in the El Niño basin and 193 grid points outside this domain. Following ref. 33, we consider at each node k the daily atmospheric temperature anomalies $T_k(t)$ (actual temperature value minus climatological average for each calendar day) at

Author contributions: A.B., S.H., and H.J.S. designed research; J.L., A.G., and M.I.B. performed research; A.G. and M.I.B. contributed new reagents/analytic tools; J.L. analyzed data; and A.B., S.H., and H.J.S. wrote the paper.

The authors declare no conflict of interest.

[1]To whom correspondence should be addressed. E-mail: john@pik-potsdam.de.

This article contains supporting information online at www.pnas.org/lookup/suppl/doi:10.1073/pnas.1309353110/-/DCSupplemental.

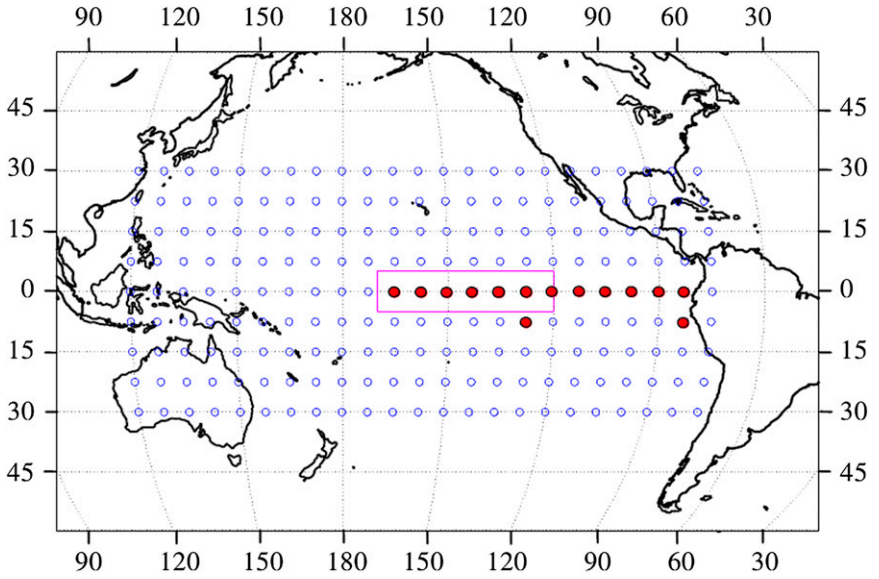

Fig. 1. The "climate network". Each node inside the El Niño basin (solid red symbols) is linked to each node outside the basin (open symbols). The nodes are characterized by their air temperature at the surface level (SAT), and the link strength between the nodes is determined from their cross-correlation. The red rectangle denotes the area where the NINO3.4 index is measured. For the definition of the El Niño basin, we have followed refs. 32 and 33. In *SI Appendix*, we provide a sensitivity test for this choice and show, for example, that the inclusion of the two nodes south of the Equator is not essential for our results.

the surface area level. The data have been obtained from the National Centers for Environmental Prediction/National Center for Atmospheric Research Reanalysis I project (35, 36).

For obtaining the time evolution of the strengths of the links between the nodes i inside the El Niño basin and the nodes j outside we compute, for each 10th day t in the considered time span between 1950 and 2011, the time-delayed cross-covariance function defined as $C_{i,j}^{(t)}(-\tau) = \langle T_i(t)T_j(t-\tau)\rangle - \langle T_i(t)\rangle\langle T_j(t-\tau)\rangle$ and $C_{i,j}^{(t)}(\tau) = \langle T_i(t-\tau)T_j(t)\rangle - \langle T_i(t-\tau)\rangle\langle T_j(t)\rangle$, where the brackets denote an average over the past 365 d, according to $\langle f(t)\rangle = \frac{1}{365}\sum_{m=0}^{364} f(t-m)$. We consider time lags τ between 0 and 200 d, where a reliable estimate of the background noise level can be guaranteed. Finally, we divide the cross-covariances by the corresponding standard deviations (SD) of T_i and T_j, to obtain the cross-correlations. Note that for estimating the cross-correlation function at day t, only temperature data from the past are considered. A representative example of $C_{ij}^{(t)}(\tau)$ is shown in *SI Appendix*, Fig. S4.

Next we determine, for each point in time t, the maximum, the mean, and the SD of $C_{ij}^{(t)}(\tau)$ around the mean and define the link strength $S_{ij}(t)$ as the difference between the maximum and the mean value, divided by the SD. Accordingly, $S_{ij}(t)$ describes the link strength at day t relative to the underlying background and thus quantifies the dynamical teleconnections between nodes i and j. We obtain the desired mean strength $S(t)$ of the dynamical teleconnections in the climate network by simply averaging over all individual link strengths. In this average, we do not weight nodes from different latitudes according to their density, because the range of such weights varies insignificantly for the narrow range of latitudes depicted in our network.

Fig. 2 shows the time evolution of $S(t)$ between January 1, 1950 and December 31, 2011. To statistically validate our method, we have divided this time interval into two equal parts. The first part (up to December 31, 1980) (Fig. 2*A*) is used for learning the optimum prediction algorithm. In the second part (from January 1, 1981 to December 31, 2011) (Fig. 2*B*) we apply this algorithm to predict the El Niño episodes. Fig. 2 compares the time dependence of $S(t)$ (left scale) with the standard NINO3.4 index (right scale). The El Niño episodes where the index is above 0.5 °C for at least 5 mo are marked in blue. Fig. 2 shows that during an El Niño event, the mean strength S of the interactions tends to decrease, supporting the hypothesis that the El Niño basin tends to decouple from the rest of the globe when the anomalous warming is in full swing (33).

More relevant, from the perspective of forecasting, is the finding that well before an episode $S(t)$ tends to increase; i.e., the cooperativity between the El Niño basin and the surrounding sites in the Pacific area grows. This feature is used here for predicting the start of an El Niño event in the following year. To this end, we place a varying horizontal threshold $S(t) = \Theta$ in Fig. 2*A* and mark an alarm when $S(t)$ crosses the threshold from below, outside an El Niño episode (i.e., when the NINO3.4 index is below 0.5 °C). We assume that such an alarm forecasts an El Niño to develop in the following calendar year. If there are multiple alarms in the same calendar year, only the first one is regarded. The alarm results in a correct prediction, if in the following calendar year an El Niño episode actually sets in; otherwise it is regarded as a false alarm.

For illustrating the algorithm, we shifted the $S(t)$ curve in Fig. 2 vertically such that the El Niño threshold (0.5 °C) coincides with our chosen threshold (here $\Theta = 2.82$). Correct predictions are marked by green arrows and false alarms by dashed arrows. Between 1951 and 1980, there are 10 y where an El Niño episode started (i.e., there are 10 events) and 20 y where it did not start (i.e., there are 20 nonevents). In Fig. 2, we see 7 correct predictions and 2 false alarms, giving rise to the hit rate 7/10 and the false-alarm rate 2/20, respectively. By altering the magnitude of the threshold, we vary the hit rate and the false-alarm rate. Fig. 3*A* shows, again for the learning period between 1950 and 1980, the best hit rates for the (tolerable) false-alarm rates 0, 1/20, 2/20, and 3/20. The best performances are for thresholds Θ in the interval between 2.805 and 2.822, where the false-alarm rate is 2/20 and the hit rate is 0.7, and for thresholds between 2.780 and 2.792, where the false-alarm rate is 3/20 and the hit rate is 0.8.

For demonstrating that these results are not accidental, we analyzed randomized $S(t)$ curves obtained by reshuffling the temperature records at each site. We randomized the calendar years but not the data within each calendar year. In this way we preserved the short-term memory in each record but reduced the cross-correlations between them. We considered 100 such randomizations and determined for each of them, for the false-alarm rates 0, 1/20, 2/20, and 3/20, respectively, the best hit rates.

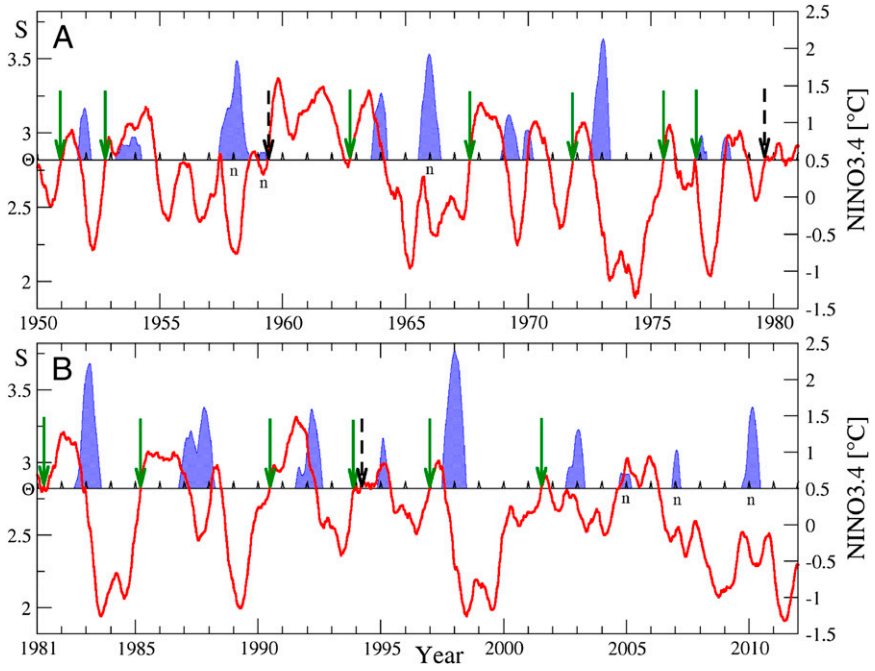

Fig. 2. The forecasting algorithm. We compare the average link strength $S(t)$ in the climate network (red curve) with a decision threshold Θ (horizontal line, here $\Theta = 2.82$) (left scale) with the standard NINO3.4 index (right scale), between January 1, 1950 and December 31, 2011. When the link strength crosses the threshold from below, outside an El Niño episode, we give an alarm and predict that an El Niño episode will start in the following calendar year. The El Niño episodes (when the NINO3.4 index is above 0.5 °C for at least 5 mo) are shown by the solid blue areas. The first half of the record (*A*) is the learning phase where we optimize the decision threshold. In the second half (*B*), we use the threshold obtained in *A* to predict El Niño episodes. Correct predictions are marked by green arrows and false alarms by dashed arrows. The index n marks a nonpredicted El Niño episode. To resolve by eye the accurate positions of the alarms, we show in *SI Appendix*, Fig. S5 magnifications of those parts of Fig. 2 where the crossings or noncrossings are difficult to see clearly without magnification. We also show the alarms for the slightly smaller threshold $\Theta = 2.81$ (*SI Appendix*, Fig. S6), which yields the same performance in the learning phase and one more false alarm in the prediction phase. The lead time between the prediction and the beginning of the El Niño episodes is 0.94 ± 0.44 y, whereas the lead time to the maximal NINO3.4 value is 1.4 ± 0.33 y.

To characterize the distribution of the best hit rates, we calculated their mean and SD. The results, also shown in Fig. 3*A*, are well below the hit rates achieved with the observational $S(t)$ curve.

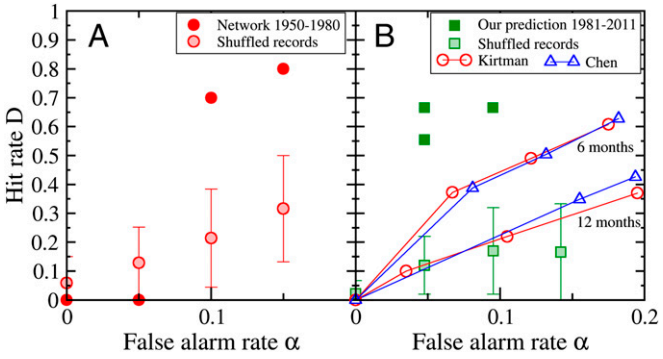

Fig. 3. The prediction accuracy [Receiver Operating Characteristic (ROC)-type analysis]. (*A*) For the four lowest false-alarm rates $\alpha = 0$, 0.05, 0.1, and 0.15, the best hit rates D in the learning phase (Fig. 2*A*). The best results are obtained at $\alpha = 0.1$ and 0.15. For $\alpha = 0.1$, the decision threshold Θ is between 2.805 and 2.822. For $\alpha = 0.15$, Θ is between 2.780 and 2.792. The results for the randomized $S(t)$ with error bars are shown as shaded circles. (*B*) The quality of the prediction in the second half of the record, when the above thresholds are applied. For $2.816 < \Theta \leq 2.822$, we have $D = 0.667$ at $\alpha = 0.048$; for $2.805 < \Theta \leq 2.816$, we have $D = 0.667$ at $\alpha = 0.095$; and for $2.780 < \Theta \leq 2.792$, we have $D = 0.556$ at $\alpha = 0.048$. For comparison, we show also results for 6- and 12-mo forecasts based on climate models (21, 37). The shaded squares and the error bars denote the mean hit rates and their SDs for predictions based on the shuffled data.

Next, we use the thresholds selected in the learning phase to predict El Niño episodes in the second half of the dataset between 1982 and 2011, where we have 9 episodes and 21 non-episodes. For Θ between 2.816 and 2.822, which is depicted in Fig. 2*B*, the hit rate is $D = 6/9 \cong 0.667$—at a false-alarm rate $\alpha = 1/21 \cong 0.048$. For Θ between 2.805 and 2.816, the hit rate is also $D = 6/9$, but the false-alarm rate is $\alpha = 2/21 \cong 0.095$. For $2.780 < \Theta \leq 2.792$, we have $D = 5/9 \cong 0.556$ at $\alpha = 1/21 \cong 0.048$. These results are highly significant because the prediction efficiency is considerably better than for the shuffled data.

For comparison, we show also the results for 6- and 12-mo forecasts based on state-of-the-art climate models (21, 37). In ref. 21, an ensemble of model trajectories has been used, whereas for the forecast of ref. 37, only a single trajectory has been used. In both references, the forecast has been compared with the NINO3.4 index, as in the current analysis. Fig. 3*B* shows that the method suggested here for predicting El Niño episodes more than 1 y ahead considerably outperforms the conventional 6-mo and 1-y forecasts. It should be noted that although one can tune lead time and robustness in physical models, this is not possible in our statistical predictions. In contrast to physical models, which predict the SST values in the relevant regions and use them for a forecast of El Niño, our algorithm instead employs the precursors in the dynamical strength of the teleconnections in the climate network to predict the onset of the warming.

Our results suggest that for enabling local perturbations of the environment to instigate an El Niño event, the network needs to be in a "cooperative" state that can be characterized, to a certain extent, by sufficiently large link strengths in the considered climate network. The cooperativity sets in well before the spring barrier and thus allows for an early forecasting of ENSO. This

situation might be related to the mechanism suggested in ref. 38 for optimal SST growth, which is essentially the emergence of a certain spatial SST pattern, resembling our finding of a cooperated fluctuation.

To study the robustness of the forecasting algorithm with respect to the underlying network structure, we varied the size of the El Niño basin by (*i*) eliminating the grid point below the equator in the middle of the Pacific (thus identifying the El Niño basin with the union of NINO1, NINO2, NINO3, and NINO3.4 regions) and (*ii*) equating the El Niño basin with the NINO1, NINO2, NINO3, and NINO4 regions (thus raising the number of the grid points in the basin to 17). In addition, we diluted the network by connecting only 20% of the surrounding nodes with the El Niño basin. We found that with all these modifications the performance of the forecasting algorithm was only slightly reduced (*SI Appendix*, Figs. S7–S11). We also tested the performance of the algorithm when the outer grid points are not in the Pacific region but in Europe. The performance of this network (*SI Appendix*, Fig. S12) was considerably weaker and comparable with the incumbent 12-mo forecasts (Fig. 3). Finally, we tested whether our algorithm can also forecast high levels (above the SD) of the negative standard southern oscillation index (SOI), which is strongly correlated to the NINO3.4 index (see, e.g., ref. 39). In contrast to the NINO3.4 index, the SOI uses atmospheric data, the pressure difference between Tahiti and Darwin. In *SI Appendix*, Fig. S13 we show that our algorithm is also able to forecast high levels of the negative SOI, with a hit rate close to 0.67 at a false alarm rate close to 0.17.

In summary, we propose a climate-network approach to forecast El Niño episodes about 1 y ahead. Our approach is based on the dynamic fluctuations of the teleconnections (links in the network) between grid points in the El Niño basin and the rest of the Pacific. The strengths of the links are obtained from the cross-correlations between the observed sea-surface-level air temperatures in the grid points. We have shown explicitly that our method outperforms existing methods in predicting El Niño events at least 6–12 mo in advance. In contrast to the algorithms using model data, our method is exclusively based on instrumental accounts that are easily accessible. Thus, the results of this study can be straightforwardly reproduced.

We did not aim to forecast La Niña events, where the NINO3.4 index is below −0.5 °C for more than 5 mo. In a trivial forecast, one predicts that an El Niño event will be followed by a La Niña event in the next year. This simple forecast has, in the considered time window between 1950 and 2012, a hit rate close to 0.73 and a false-alarm rate close to 0.17. An even better forecast of La Niña events using the climate network requires an additional precursor to be found and is beyond the scope of this article.

Altogether, our findings indicate that El Niño is a cooperative phenomenon where the teleconnections between the El Niño basin and the rest of the Pacific tend to build up in the calendar year before an event. For characterizing the teleconnections we have used a univariate model where only one climate variable (atmospheric temperature) has been used.

Finally, we note that our algorithm (Fig. 2*B*) did correctly predict the absence of an El Niño event in 2012. This forecast was made in 2011 already, whereas conventional approaches kept on predicting the warming occurrence far into the year 2012 (40).

ACKNOWLEDGMENTS. We acknowledge financial support from the Deutsche Forschungsgemeinschaft.

1. Clarke AJ (2008) *An Introduction to the Dynamics of El Niño and the Southern Oscillation* (Academic, London).
2. Sarachik ES, Cane MA (2010) *The El Niño-Southern Oscillation Phenomenon* (Cambridge Univ Press, Cambridge, UK).
3. Dijkstra HA (2005) *Nonlinear Physical Oceanography: A Dynamical Systems Approach to the Large Scale Ocean Circulation and El Niño* (Springer Science, New York).
4. Wang C, et al. (1996) El Niño and Southern Oscillation (ENSO): A review. *Coral Reefs of the Eastern Pacific*, eds Glymn P, Manzello D, Enochs I (Springer, Berlin).
5. Brönnimann S, et al. (2004) Extreme climate of the global troposphere and stratosphere in 1940-42 related to El Niño. *Nature* 431(7011):971–974.
6. Wen C (2002) Impacts of El Niño and La Niña on the cycle of the East Asian winter and summer monsoon. *Chin J Atmos Sci* 5:595–610.
7. Corral A, Ossó A, Llebot JE (2010) Scaling of tropical-cyclone dissipation. *Nat Phys* 6:693–696.
8. Donnelly JP, Woodruff JD (2007) Intense hurricane activity over the past 5,000 years controlled by El Niño and the West African monsoon. *Nature* 447(7143):465–468.
9. Kovats RS, Bouma MJ, Hajat S, Worrall E, Haines A (2003) El Niño and health. *Lancet* 362(9394):1481–1489.
10. Davis M (2001) *Late Victorian Holocausts: El Niño Famines and the Making of the Third World* (Verso, London).
11. Solomon S, et al., eds (2007) *Climate Change 2007: The Physical Science Basis* (Cambridge Univ Press, Cambridge, UK).
12. Schellnhuber HJ, et al., eds (2006) *Avoiding Dangerous Climate Change* (Cambridge Univ Press, Cambridge, UK).
13. Lenton TM, et al. (2008) Tipping elements in the Earth's climate system. *Proc Natl Acad Sci USA* 105(6):1786–1793.
14. Schellnhuber HJ (2009) Tipping elements in the Earth system. *Proc Natl Acad Sci USA* 106(49):20561–20563.
15. Latif M, Keenlyside NS (2009) El Nino/Southern Oscillation response to global warming. *Proc Natl Acad Sci USA* 106(49):20578–20583.
16. Cane MA, Zebiak SE, Dolan SC (1986) Experimental forecasts of El Niño. *Nature* 321:827–832.
17. Latif M, et al. (1994) A review of ENSO prediction studies. *Clim Dyn* 9(4-5):167–179.
18. Tziperman E, Scher H (1997) Controlling spatiotemporal chaos in a realistic El Nino prediction model. *Phys Rev Lett* 79:1034–1037.
19. Kirtman BP, Schopf PS (1998) Decadal variability in ENSO predictability and prediction. *J Clim* 11:2804–2822.
20. Landsea CW, Knaff JA (2000) How much skill was there in forecasting the very strong 1997–98 El Niño? *Bull Am Meteorol Soc* 81:2107–2119.
21. Kirtman BP (2003) The COLA anomaly coupled model: Ensemble ENSO prediction. *Mon Weather Rev* 131:2324–2341.
22. Fedorov AV, Harper SL, Philander SG, Winter B, Wittenberg A (2003) How predictable is El Niño? *Bull Am Meteorol Soc* 84:911–919.
23. Müller P, von Storch H (2004) *Computer Modelling in Atmospheric and Oceanic Sciences* (Springer, Berlin).
24. Chen D, Cane MA, Kaplan A, Zebiak SE, Huang D (2004) Predictability of El Niño over the past 148 years. *Nature* 428(6984):733–736.
25. Palmer T, Hagedorn R (2006) *Predictability of Weather and Climate* (Cambridge Univ Press, Cambridge, UK).
26. Luo JJ, Masson S, Behera SK, Yamagata T (2008) Extended ENSO predictions using a fully coupled ocean–atmosphere model. *J Clim* 21(1):84–93.
27. Yeh SW, et al. (2009) El Niño in a changing climate. *Nature* 461(7263):511–514.
28. Chekroun MD, Kondrashov D, Ghil M (2011) Predicting stochastic systems by noise sampling, and application to the El Niño-Southern Oscillation. *Proc Natl Acad Sci USA* 108(29):11766–11771.
29. Galanti E, Tziperman E, Harrison M, Rosati A, Sirkes Z (2003) A study of ENSO prediction using a hybrid coupled model and the adjoint method for data assimilation. *Mon Weather Rev* 131:2748–2764.
30. Goddard L, et al. (2001) Current approaches to seasonal to interannual climate predictions. *Int J Clim* 21:1111–1152.
31. Tsonis AA, Swanson KL, Roebber PJ (2006) What do networks have to do with climate? *Bull Am Meteorol Soc* 87:585–595.
32. Yamasaki K, Gozolchiani A, Havlin S (2008) Climate networks around the globe are significantly affected by El Niño. *Phys Rev Lett* 100(22):228501.
33. Gozolchiani A, Havlin S, Yamasaki K (2011) Emergence of El Niño as an autonomous component in the climate network. *Phys Rev Lett* 107(14):148501.
34. Tsonis AA, Swanson KL (2008) Topology and predictability of El Niño and La Niña networks. *Phys Rev Lett* 100(22):228502.
35. National Oceanic and Atmospheric Administration, Earth System Research Laboratory. Available at http://www.esrl.noaa.gov/psd/data/gridded/data.ncep.reanalysis.html. Accessed September 23, 2012.
36. Kalnay E, et al. (1996) The NCEP/NCAR 40-year reanalysis project. *Bull Am Meteorol Soc* 77:437–471.
37. Chen D, Cane MA (2008) El Nino prediction and predictability. *J Comput Phys* 227:3625–3640.
38. Penland C, Sardeshmukh PD (1995) The optimal growth of tropical sea surface temperature anomalies. *J Clim* 8:1999–2024.
39. Dijkstra HA (2006) The ENSO phenomenon: Theory and mechanisms. *Adv Geosci* 6:3–15.
40. National Oceanic and Atmospheric Administration, National Centers for Environmental Prediction. Available at http://www.cpc.ncep.noaa.gov/products/analysis_monitoring/enso_advisory/. Accessed August 20, 2012.

Supporting Information: "Improved El Niño Forecasting by Cooperativity Detection"

by J. Ludescher, A. Gozolchiani, M.I. Bogachev,
A. Bunde, S. Havlin and H.-J. Schellnhuber

May 23, 2013

In this supplemental material, we show

(i) a typical example of the cross-covariance function $C_{ij}(t;\tau)$ between two nodes in the considered climate network (Fig. 4). The strength of the link between two nodes is determined as the maximum of the cross-covariance C_{ij}^{max} divided by its standard deviation in the time window with $|\tau| \leq 200$. The average strength of the links in the climate network is determined by averaging over all possible links between the nodes inside and outside of the El Niño basin;

(ii) magnifications of those parts of Fig. 2 in the Letter where the average link strength $S(t)$ in the climate network (red curve) is close to the decision threshold Θ and the crossings or non-crossings are difficult to see clearly without magnification (Fig. 5). In addition we also show the result for the slightly smaller threshold $\Theta = 2.81$ (Fig. 6), which yields the same performance in the learning phase and one more false alarm in the prediction phase.

(iii) two examples of the networks with modified definition of the El Niño basin, including 13 grid points (Fig. 7) and 17 grid points (Fig. 8), and the prediction efficiency. The figures show the robustness of the El Niño prediction algorithm to the modifications in the network structure and in particluar to the choice of the El Niño basin;

(iv) three representative examples of the diluted climate networks with elimination of 80% of the nodes outside of the El Niño basin (Figs. 9 – 11) and the prediction efficiency. The figures show the robustness of the El Niño prediction algorithm to the incompleteness of the data and the choice of grid points from the outside basin;

(v) an example of the climate network, where the outside basin consists of grid points from the European instead of the Pacific region (Fig. 12) and the prediction efficiency. The figure shows that in this case the efficiency of forecasting El Niño, contrast to the various configurations of the Pacific network, is considerably reduced;

(vi) application of the algorithm to predict when the negative (standardized) southern oscillation index (SOI) defined as the difference between the (standardized) pressure of Darwin and the (standardized) pressure of Tahiti exceeds its standard deviation. It is well known that the negative SOI is strongly correlated with the NINO3.4 index. In Fig. 13 we show that our algorithm to forecast El Niño episodes can also be used to forecast the high levels of the SOI.

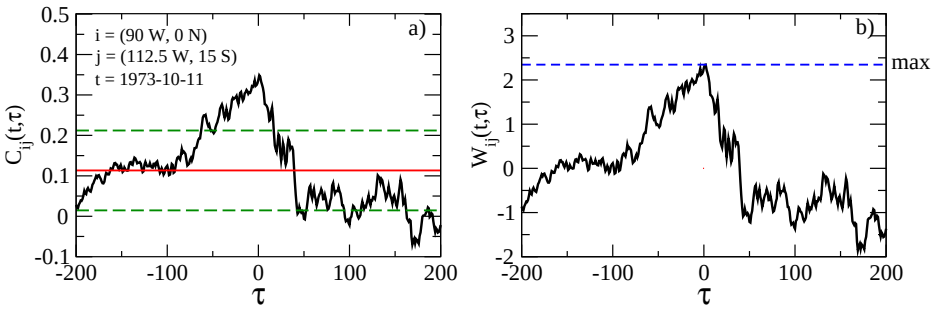

Figure 4: (a) A representative example of the cross-covariance $C_{ij}(t;\tau)$ function between two nodes in the climate network. The horizontal red line shows the mean value, the horizontal green dashed lines show the standard deviation. (b) The normalized cross-covariance W_{ij} defined as $C_{ij}(t;\tau)$ with subtracted mean and divided by the standard deviation. The maximum value in (b) denotes the link strength.

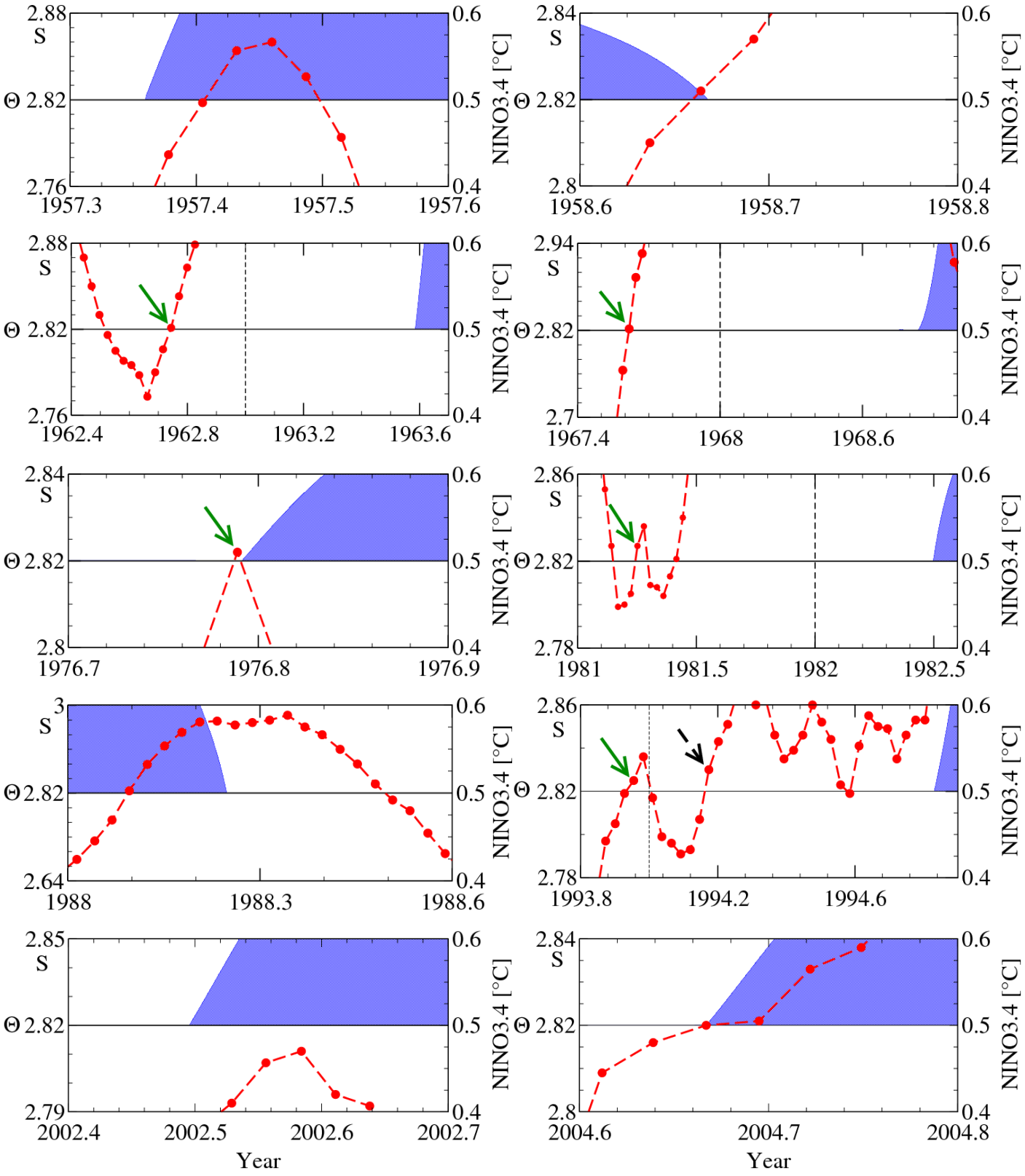

Figure 5: The magnifications of the S(t) curve (see Fig. 2 in the Letter) at the crossing points for the threshold Θ = 2.82. True alarms are marked by green arrows and false alarms by dashed arrows.

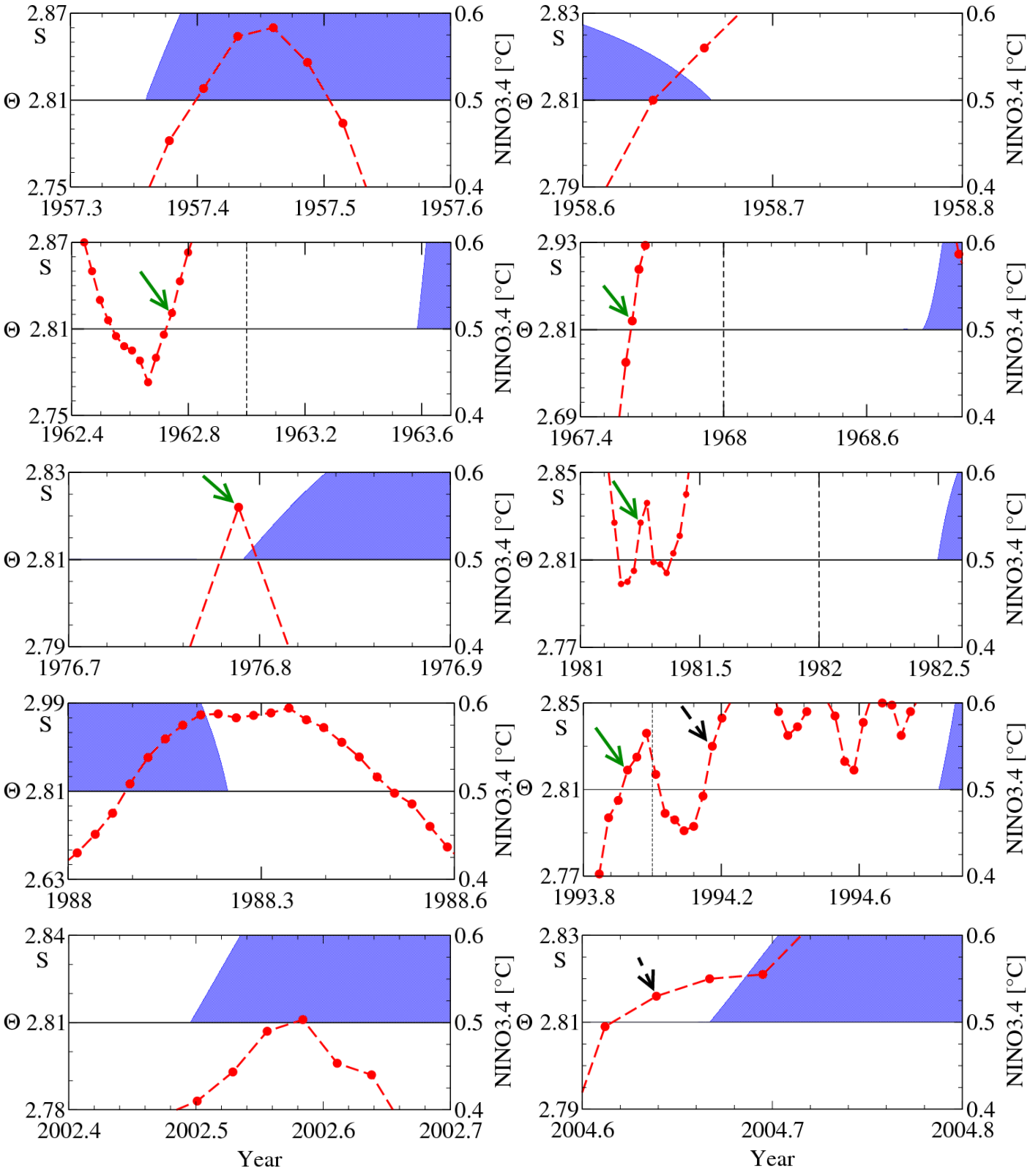

Figure 6: The magnifications of the S(t) curve (see Fig. 2 in the Letter) at the crossing points for the threshold Θ = 2.81. True alarms are marked by green arrows and false alarms by dashed arrows.

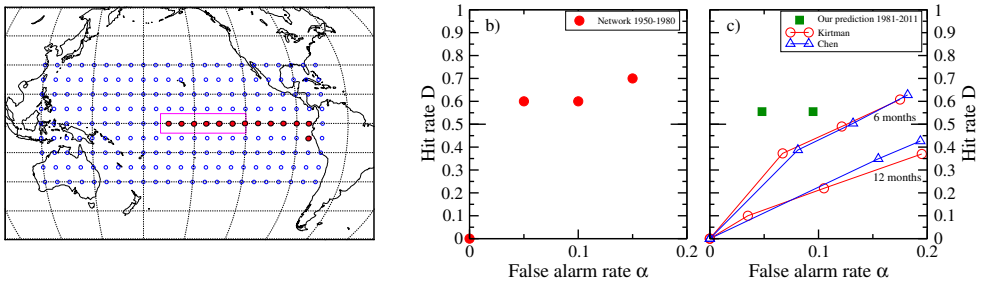

Figure 7: (a) A climate network modification, where the El Niño basin consisting of the NINO 1, 2, 3 and 3.4 regions (red symbols) is linked to the nodes in the Pacific outside the basin (open symbols) (compare with Fig. 1 in the Letter). (b) shows for the four lowest false alarm rates α, the best hit rates D in the learning phase (compare with Fig. 3a in the Letter). The best results are obtained at $\alpha = 0.05$ and 0.15. For $\alpha = 0.05$, the decision threshold Θ is between 2.804 and 2.817. For $\alpha = 0.15$, Θ is between 2.710 and 2.716. (c) shows the quality of the prediction in the second half of the record, when the above thresholds are applied. For $2.804 < \Theta \leq 2.817$, we have $D = 5/9$ at $\alpha = 1/21$, for $2.710 < \Theta \leq 2.716$, we have $D = 5/9$ at $\alpha = 2/21$. For comparison, we show also results for 6- and 12-months forecasts based on climate models (compare with Fig. 3b in the Letter).

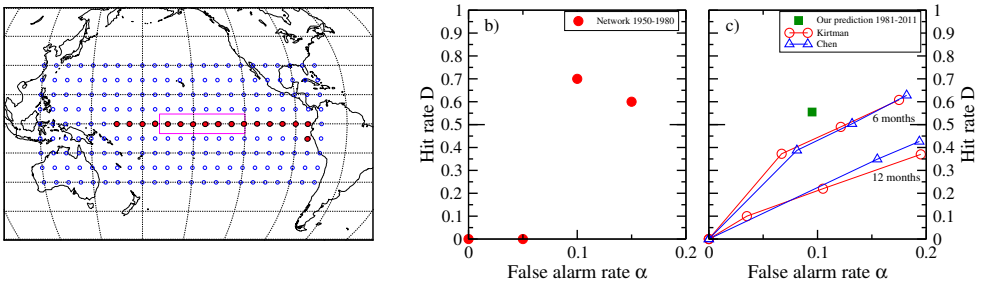

Figure 8: (a) A climate network modification, where the El Niño basin consisting of the NINO 1, 2, 3 and 4 regions (red symbols) is linked to the nodes in the Pacific outside the basin (open symbols) (compare with Fig. 1 in the Letter). (b) shows for the four lowest false alarm rates α, the best hit rates D in the learning phase (compare with Fig. 3a in the Letter). The best result is obtained at $\alpha = 0.1$, when the decision threshold Θ is between 2.828 and 2.838. (c) shows the quality of the prediction in the second half of the record. When the above thresholds are applied, we have $D = 5/9$ at $\alpha = 2/21$. For comparison, we show also results for 6- and 12-months forecasts based on climate models (compare with Fig. 3b in the Letter).

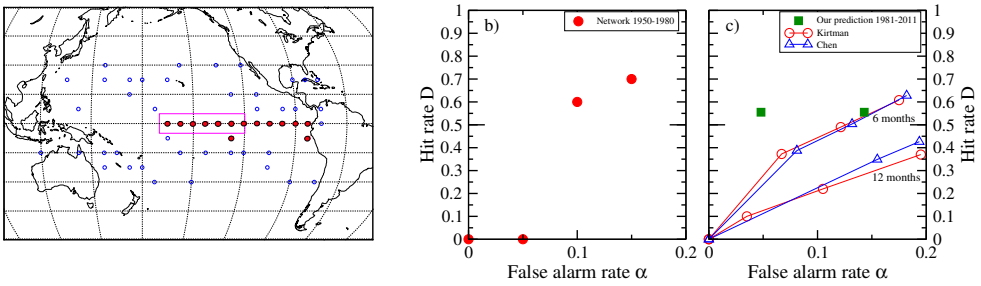

Figure 9: (a) A diluted climate network, where the El Niño basin (red symbols) is linked to the 20% of the randomly selected nodes in the Pacific outside the basin (open symbols). (compare with Fig. 1 in the Letter) (b) shows for the four lowest false alarm rates α, the best hit rates D in the learning phase (compare with Fig. 3a in the Letter). The best results are obtained at $\alpha = 0.1$ and 0.15. For $\alpha = 0.1$, the decision threshold Θ is between 2.939 and 2.948. For $\alpha = 0.15$, Θ is between 2.874 and 2.889. (c) shows the quality of the prediction in the second half of the record, when the above thresholds are applied. For $2.939 < \Theta \leq 2.948$, we have $D = 5/9$ at $\alpha = 1/21$, for $2.874 < \Theta \leq 2.889$, we have $D = 5/9$ at $\alpha = 3/21$. For comparison, we show also results for 6- and 12-months forecasts based on climate models (compare with Fig. 3b in the Letter).

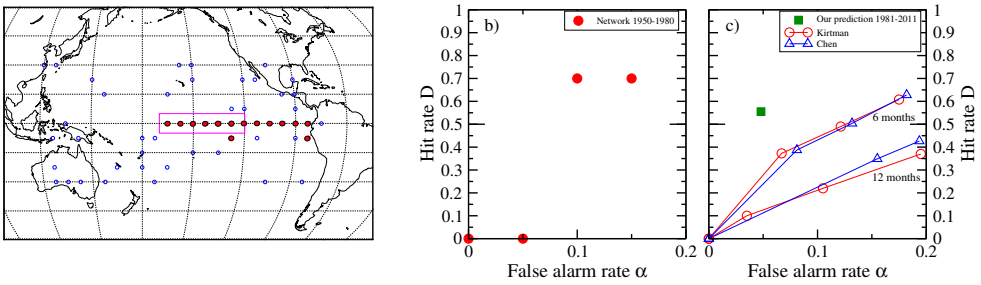

Figure 10: (a) A diluted climate network, where the El Niño basin (red symbols) is linked to the 20% of the randomly selected (configuration 40 out of 100) nodes in the Pacific outside the basin (open symbols) (compare with Fig. 1 in the Letter). (b) shows for the four lowest false alarm rates α, the best hit rates D in the learning phase (compare with Fig. 3a in the Letter). The best result is obtained at $\alpha = 0.1$, when the decision threshold Θ is between 2.783 and 2.798. (c) shows the quality of the prediction in the second half of the record, when the above thresholds are applied, we have $D = 5/9$ at $\alpha = 1/21$. For comparison, we show also results for 6- and 12-months forecasts based on climate models (compare with Fig. 3b in the Letter).

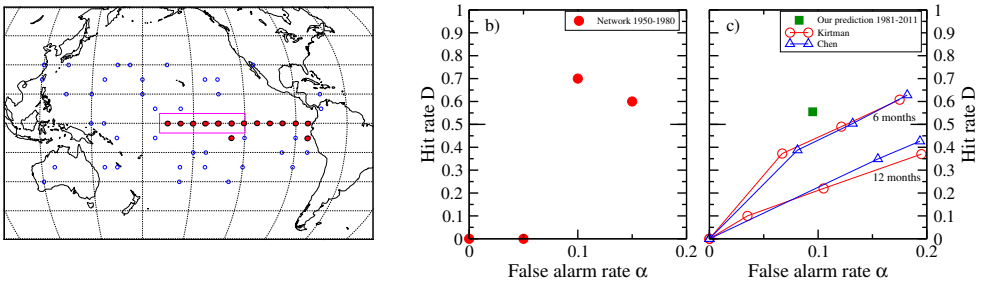

Figure 11: (a) A diluted climate network, where the El Niño basin (red symbols) is linked to the 20% of the randomly selected nodes (configuration 83 out of 100) in the Pacific outside the basin (open symbols) (compare with Fig. 1 in the Letter). (b) shows for the four lowest false alarm rates α, the best hit rates D in the learning phase (compare with Fig. 3a in the Letter). The best result is obtained at $\alpha = 0.1$, when the decision threshold Θ is between 2.783 and 2.807. (c) shows the quality of the prediction in the second half of the record, when the above thresholds are applied, we have $D = 5/9$ at $\alpha = 2/21$. For comparison, we show also results for 6- and 12-months forecasts based on climate models (compare with Fig. 3b in the Letter).

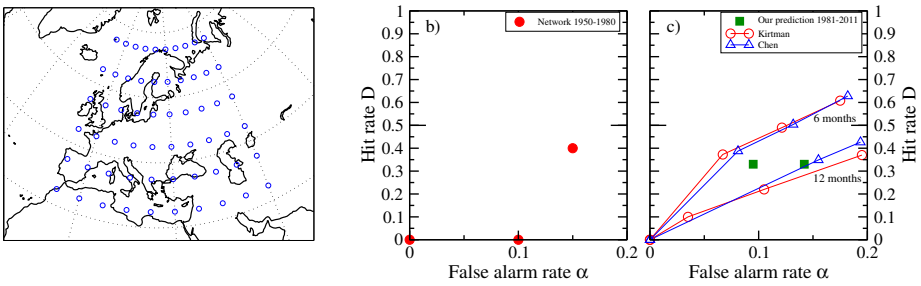

Figure 12: (a) A climate network modification, where the El Niño basin (similar to the basin in Fig. 1 of the Letter) is linked to the nodes in the European region instead of the Pacific region (open symbols) (compare with Fig. 1 in the Letter). (b) shows for the four lowest false alarm rates α, the best hit rates D in the learning phase (compare with Fig. 3a in the Letter). The best results are obtained at $\alpha = 0.15$, when the decision threshold Θ is between 3.381 and 3.395. (c) shows the quality of the prediction in the second half of the record, when the above thresholds are applied. For $3.381 < \Theta \leq 3.388$, we have $D = 3/9$ at $\alpha = 2/21$, for $3.388 < \Theta \leq 3.395$, we have $D = 3/9$ at $\alpha = 3/21$. For comparison, we show also results for 6- and 12-months forecasts based on climate models (compare with Fig. 3b in the Letter).

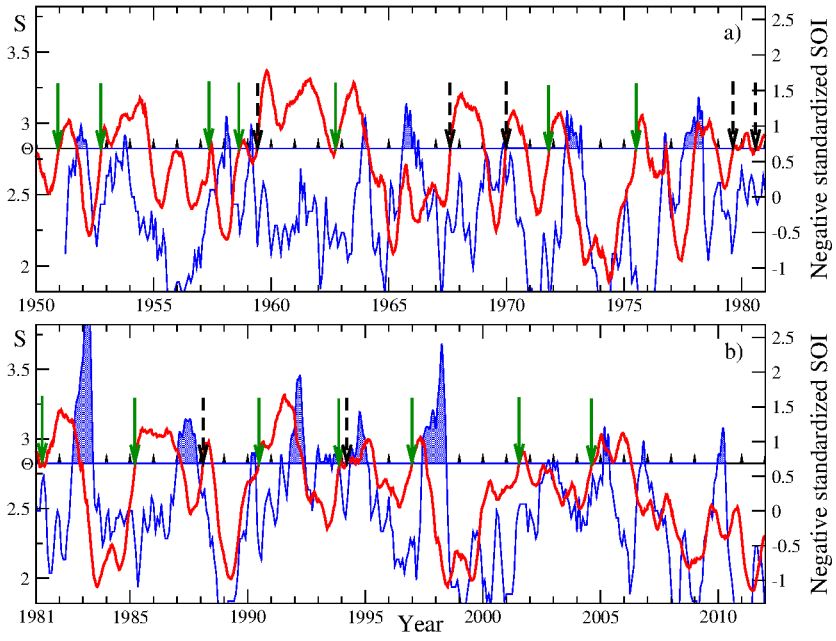

Figure 13: Similar to Fig. 2 in the Letter, but for the mean link strength $S(t)$ (red, the same as in Fig. 2) and the negative (standardized) southern oscillation index (blue). The threshold Θ is the same as in Fig. 2. We aim to predict episodes where the negative SOI is above its standard deviation. When the link strength crosses the threshold from below, we give an alarm. As in Fig. 2, green arrows mark correct predictions, while the black dashed arrows mark the false alarms. From the figure, we obtain a hit rate $D = 14/21 \cong 0.67$ at a false alarm rate $\alpha = 7/41 \cong 0.17$.